Characterization of Electrostatic Discharges induced Plasmas in dielectrics irradiated by multi-MeV electron beam

Tristan Gouriou, Maxime Ribière, Jérémie-Marie Plewa, R. Maisonny, Olivier Cessennat, Olivier Eichwald, Mohammed Yousfi

Characterization of electrostatic discharge induced plasmas in dielectrics irradiated by multi-MeV electron beam

Cite as: Phys. Plasmas **27**, 013502 (2020); https://doi.org/10.1063/1.5127814
Submitted: 19 September 2019 • Accepted: 14 December 2019 • Published Online: 14 January 2020

T. Gouriou, M. Ribière, J.-M. Plewa, et al.

Physics of Plasmas ARTICLE scitation.org/journal/php

Characterization of electrostatic discharge induced plasmas in dielectrics irradiated by multi-MeV electron beam

Cite as: Phys. Plasmas **27**, 013502 (2020); doi: 10.1063/1.5127814
Submitted: 19 September 2019 · Accepted: 14 December 2019 ·
Published Online: 14 January 2020

T. Gouriou,[1,2,a)] M. Ribière,[1] J.-M. Plewa,[1,2] R. Maisonny,[1] O. Cessenat,[3] O. Eichwald,[2] and M. Yousfi[2]

AFFILIATIONS

[1]CEA, DAM, GRAMAT, F-46500 Gramat, France
[2]LAPLACE, CNRS, University of Toulouse, 118 Route de Narbonne, F-31062 Toulouse, France
[3]CEA/DAM/CESTA, F-33405 Le Barp, France

[a)]Electronic address: tristan.gouriou@cea.fr

ABSTRACT

This work is devoted to experimental analyses of plasmas induced by electrostatic discharges in dielectric materials. Electrostatic discharges are produced in polytetrafluoroethylene (Teflon) and polyethylene samples irradiated by a 6-MeV electron beam generated by a linear accelerator facility. The time and space evolution of the conductivity of the plasma is determined by microwave transmission measurements across a cavity followed by comparison with 3D Maxwell calculations. Furthermore, plasma parameters such as average electron energies and densities of electrons and neutral background species are determined from a 0D collisional radiative model. This analysis infers a plasma expansion velocity of about 150 km/s and a maximum electric conductivity of about 40 S/m. The electron density is estimated to be about 10^{12} cm^{-3}, and electron average energies are up to 60 eV, while neutral species densities do not exceed 10^{18} cm^{-3}.

I. INTRODUCTION

The objective of this work is to provide quantitative information on ESD-induced plasmas produced by dielectric breakdown following internal charging by electron implantation in dielectrics. These effects can occur in satellites as well as in a broad range of electronic parts integrated within diagnostics used while operating facilities such as nuclear power plants, particle accelerators,[1] high energy,[2] high power[3] laser beams, and high pulsed power electron or X-ray beams.[4–7] These ESDs may significantly affect the electric signals associated with the measurements, thus inducing misinterpretation. ESDs may also induce thermomechanical degradation.

Spacecraft crossing radiation belts can experience ESD, which are known as a major cause of satellite anomalies.[8,9] In addition to the mechanical degradation of the irradiated material, ESDs produce an electromagnetic pulse (EMP) that can disturb or damage spacecraft electronics such as scientific measurements, communication and navigation systems, and so on. Typical dielectric materials in satellites are Kapton, FR4, Mylar, PolyEtherEtherKetone (PEEK), or Teflon.[10–12] These dielectrics are constitutive of thermal blankets, coaxial cables, printed circuit boards, connectors, etc. Dielectric charging and induced ESD can be reproduced in the laboratory with an electron gun or a particle accelerator.[13] ESDs come from the entrapment of high-energy electrons delivered by the accelerator deeply deposited inside the material. Electron accumulation leads to high internal electric fields up to the disruptive threshold. Breakdown occurs locally, in the vicinity of a defect in the dielectric bulk. From this defect location, a channel of ionized species develops into the dielectric extremely rapidly and is associated with a large electron current density, which leads to the production of an electromagnetic pulse[14] and a plasma. Plasma analysis is important to provide an accurate understanding and restitution of the electromagnetic pulse and replacement currents induced by ESD.

Therefore, in order to quantify the effects of ESD, an experimentally accelerated aging approach is performed in this work by imposing the magnitude of the dose rate in the dielectric in order to quickly reach the disruptive threshold of dielectric samples. This approach based on accelerated aging allows for numerous acquisitions and statistical analysis of the ESD and is motivated by the fact that predicting the occurrence of ESD is very difficult because it requires the accurate knowledge of (i) the electron flux impinging the electronics, (ii) the disruptive thresholds of each irradiated dielectric, which are related to manufacturing processes and microscopic defects, and furthermore, (iii) the radiation induced conductivity (RIC) aging and recovering of each dielectric.[15]

Also, concerning the electronics on spacecraft, the prediction of ESD (occurrence rates and levels) also requires the accurate knowledge of the electron flux and spectrum in the space environment. Consequently, the calculations of ESD characteristics may lead to uncertain predictions, and despite many studies on charging processes, ESD still remains an issue for spacecraft reliability. So, as a complementary method, the quantification of ESD characteristics performed in this work may provide suitable information for electronic system hardening.

This work presents an analysis of ESD induced plasmas from microwave transmission measurements compared to 3D Maxwell calculations. This comparison allows for the determination of the time and space evolution of the electric conductivity of the plasma. Also, the results of a 0D collisional radiative model (CRM) are presented, and plasma parameters such as species densities and average electron energy are then inferred. The ESDs are produced by irradiation of dielectrics using a 6.17-MeV electron beam produced by a linear accelerator (LINAC).

Section II following this introduction presents the experimental setup and results. In Sec. III, 3D-Maxwell modeling is described, and Sec. IV is devoted to the results of 3D Maxwell calculations, which infers plasma conductivity. Also, the results of CRM calculations are presented in this section.

II. EXPERIMENTAL SETUP AND RESULTS

A. Experimental setup

This section is devoted to the description of the experimental setup for the measurements of time resolved ESD induced plasma electric conductivity, based on microwave transmission across a cavity.

Dielectric samples are irradiated by an electron beam produced by the linear accelerator Oriatron at CEA-Gramat. This facility has been described elsewhere[14,16] and is used to quantify the vulnerability of electronics and optics to the ionizing dose. The accelerator provides 4.5 μs monoenergetic electron pulses at 6.17 MeV with a repetition rate of up to 160 Hz in our experimental conditions, providing an average dose rate equal to 330 Gy(air)/s and 1.5 Gy(air) per pulse at one meter. The experimental setup is displayed in Fig. 1.

A stainless-steel cylindrical cavity with the length and diameter equal to 25 cm is located 120 cm from the output window of an Oriatron accelerator. At this distance, the spatial repartition of the incident electron flux impinging the cavity is homogeneous. Cylindrical ports located at 10 cm from the face located in the direct view of the electron beam provide outlets for vacuum ports and electric diagnostics. A 2-cm thick steel screen with a 30-cm hole diameter is set to protect cables dedicated to currents and field measurements. An aluminum flange located in the direct view of the electron beam is machined to collimate the electron beam on a circular disk with a diameter equal to 9 cm. The aluminum flange is 4 mm thick within this diameter and 2 cm thick outside. This insures a better protection for the B-dot and current probes from the electron flux. Electrostatic discharges were observed in polytetrafluoroethylene $(C_2F_4)_n$ (or PTFE) and polyethylene $(C_2H_4)_n$ (or PE). Air inside the cavity is evacuated by a turbomolecular pump, providing a residual air pressure below 10^{-4} mbar.

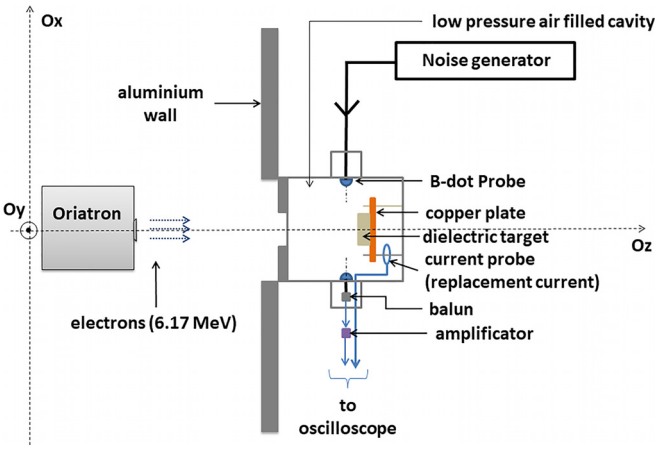

FIG. 1. Overall experimental configuration.

Dielectric samples are glued on a copper plate, while the other face is directly exposed to the electron beam. Dielectric samples have a diameter equal to 9.6 cm and a thickness of 3 cm. Three nylon rods and one stainless steel rod sustain the copper plate at 7 cm from the surface of the cavity located downstream. The thicknesses of the samples must be greater than the penetration length of the incident e-beam (which is about 2 cm in PE) in order to allow for electron implantation, internal charging, and subsequent dielectric breakdown. In space applications, the charging process of dielectrics is produced by electrons having a range of energies resulting from a compromise between abilities to go through the different materials screening the dielectric on the one hand, and electron penetration lengths lighter than dielectric thicknesses on the other hand. For example, around Jupiter, electron energies of up to 11 MeV have been reported.[17] A part of this electron flux may contribute to the charging process and subsequent ESD phenomenon if the constitutive electrons of this flux experience adequate slowing down.

Before each irradiation, a small hole is performed in the middle of the dielectric on the face in the direct view of the electron beam. This defect ensures the location of the arc site, which is suitable for the alignment of optical diagnostics (see Sec. II C), as well as for the comparison of experiments with calculations performed in Sec. IV.

As mentioned in Sec. I, the electron beam energy is equal to 6.17 MeV at the output of the accelerator. Before interacting with the dielectric target, the electron beam flux and the average energy are decreased by the vacuum/air interface of the cavity constituted by a 4 mm-thick aluminum disk. As a consequence, the electron beam impinging the dielectric can be modeled by a Gaussian profile centered at 4 MeV, with a 0.5-MeV-FWHM (full width at half maximum).[14] This experimental layout allows for a homogeneous electron flux on the dielectric sample equal to 32 nC/cm^2/s, providing a maximal dose rate equal to 35 Gy(PE)/s in the dielectric.

It is noteworthy that the current fluxes obtained with our linear accelerator are higher than the radiative constraints observed in space environment. For example, in Earth radiation belts, for 1 MeV electrons, the current densities are about picoamperes per square centimeter, while around Jupiter, it is about a nanoampere per square centimeter.[17] Nevertheless, as mentioned in the Introduction section, the dose rates put into operation in this work allow for analyzing numerous ESDs, which are suitable for statistical analysis. The high dose rate put into operation allows for a rapid increase in the electric field together with the increase in radiation-induced conductivity, which is confirmed by Monte Carlo simulation and the dose

calculation in the dielectric (see Ref. 14 for calculations in PTFE). Assuming a dose rate equal to 35 Gy(PE)/s in PE, the radiation induced conductivity can be estimated from DICTAT (Dielectric Internal Charging Threat Assessment Tool) database[18] to be about 10^{-11} S/m for PE, which is much larger than the dark conductivity (about 10^{-14} S/m). So, radiation-induced effects occur in our high dose rate experiments, due to the dose rate dependence of RIC models. Nevertheless, for spacecraft situations, the facts that the dose rate is much lower as compared to our experimental situation allow for recovering effects to occur, which may move forward the cumulative dose required to produce the ESD.

According to the high energy of the constitutive electrons of the incident e-beam, the spatial repartitions of the charge and dose rates deposited in the material occur on the centimeter scale. So, the increase in the electric field due to charge deposition may only have a little influence on electron transport and hence on the spatial repartition of charge and energy deposition. We indeed try to lower the energy of the incident e-beam by adding a 2-mm-thick aluminum screen upstream the cavity, but this only decreased the e-beam average energy from 4 to 3 MeV, and the electron penetration length from 2.1 to 1.6 cm in PE.[19] As a result, the observed effect was a reduction of the ESD occurrence rate in the same proportion as the reduction of the electron flux.

Replacement currents are measured with a probe (Pearson 8585C) having a transfer function equal to 0.5 Ω in the frequency range (0.15–250) MHz. The measurement is performed by setting the probe around the steel rod. The current probe is connected to the oscilloscope (2.5 GHz bandwidth oscilloscope, DPO 7254 from Tektronix) by an RG223 coaxial cable with a 50 Ω impedance. The electric signal measured by the current probe is split via a 6 dB signal divider and recorded on two oscilloscope channels having different calibers.

A noise generator (NC6112A from Noisecom) delivers a white Gaussian noise in the frequency band (10^{-3}–2) GHz. The output of the noise generator is coupled to a B-dot probe (Prodyn RBX30B) through an air/vacuum electric transition and produces an electromagnetic wave propagating through the cavity. The B-dot probe is laid flat onto the lateral surface of the cavity and has a derivative behavior of up to 3.5 GHz with an equivalent area equal to 5×10^{-4} m^2. A second B-dot probe is fielded onto the lateral surface of the cavity and collects the transmitted signal. This B-dot probe is connected to a balanced to an unbalanced (balun) converter (Prodyn BIB-105F-2M) in order to suppress the common parasitic coupling to each channel, hence improving the signal-to-noise ratio. The output of the balun is connected to an amplificatory (RAMP00G30GA from RF lambda) to improve the level of the collected signal. The probes are radiation hardened according to the manufacturer specifications. The probe axes are set collinear to the *Oy* (see Fig. 1).

Figures 2(a) and 2(b) show the microwave signal launched at the generator output and the Fourier analysis of the transmitted signal by the cavity without ESD induced plasma.

Figure 2(b) shows that several modes of the cavity are transmitted. As shown in Ref. 20, both the real and imaginary parts of the electric conductivity can be determined by simultaneously measuring the transmission and the shift of a single-frequency signal. However, this implies a perfect reproducibility of the plasma in the cavity, which is not the case of ESD induced plasmas. Hence, even if the frequency shift may occur in our experiment, due to the variation of plasma permittivity, this has no impact on transmission measurements, because all the frequencies are launched into the cavity with the same amplitude.

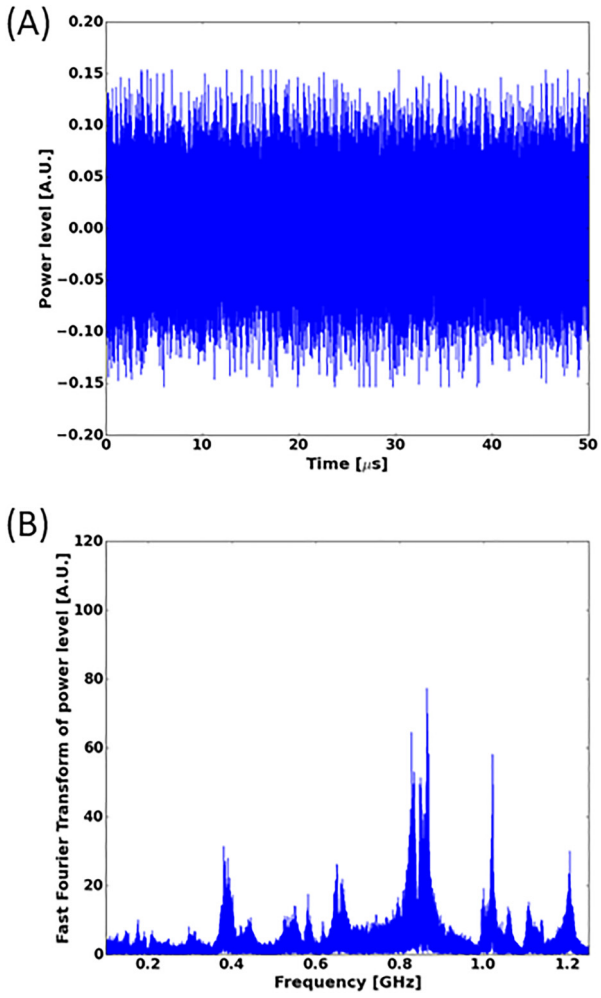

FIG. 2. (a) Microwave signal at the noise generator output launched into the cavity. (b) Fourier analysis of the signal transmitted by the cavity (without plasma).

B. Theory of electromagnetic wave absorption

The interaction of microwaves with plasmas and, more specifically, transmission, reflection, interferometry, and resonant cavity analysis are used to determine electric conductivity, and with some assumptions, the electron density and collision frequency of the plasma.[20–23] When a plasma is created in a cavity, the modification of its quality factor considering an oscillating electric field $E(r)$ is given by the following equation:

$$\left(\frac{1}{Q_1}-\frac{1}{Q_0}\right)-2j\frac{\omega_1-\omega_0}{\omega_0}=\frac{1}{\varepsilon_0\,\omega_0}\frac{\int_V \tilde{\sigma}(r,\omega)E^2(r)dr}{\int_V E^2(r)dr}, \quad (1)$$

where ε_0 is the permittivity of vacuum, Q_1 and Q_0 are the cavity of the quality factors with and without plasma, respectively, and ω_1 and ω_0 are the resonant frequencies of the considered mode with and without plasma in the cavity, respectively. The integral is calculated over the

cavity volume, and r is the position in the cavity. $\tilde{\sigma}(r,\omega) = \sigma_{re} + j\,\sigma_{im}$ is the complex electric conductivity for a weakly ionized plasma defined by

$$\tilde{\sigma}(r,\omega) = -\frac{4\pi}{3}\frac{n_e(r)\,e^2}{m_e}\int_0^\infty \frac{1}{\vartheta(v)+j\omega}\frac{df_0(v)}{dv}v^3 dv. \tag{2}$$

This expression is derived in the case of weakly ionized plasmas where binary collisions between electrons and neutrals governed momentum transfers.[23] $n_e(r)$ is the electron density, m_e is the electron mass, e is the electron charge, $f_0(v)$ is the isotropic part of the distribution function, and $\vartheta(v)$ is the collision frequency for momentum transfers depending on the momentum transfer collision cross section of carbon C and hydrogen H species with densities n_C and n_H and defined by

$$\vartheta(v) = n_C\,\sigma_C^m\,v + n_H\,\sigma_H^m\,v. \tag{3}$$

The previous relationships can be rewritten by introducing the complex permittivity of the plasma defined by $\tilde{\epsilon}_p(r,\omega) = 1 - j\frac{\tilde{\sigma}(r,\omega)}{\varepsilon_0\omega}$, which allows us to obtain

$$\left\{\frac{\Delta\omega_1}{\omega_1} - \frac{\Delta\omega_0}{\omega_0}\right\} = \frac{1}{\varepsilon_0\,\omega_0}\frac{\int_V \tilde{\sigma}_{re}\,E^2(r)dr}{\int_V E^2(r)dr} = -\frac{1}{\varepsilon_0\,\omega_0}\frac{\int_V \tilde{\epsilon}_{im}(r)\varepsilon_0\,\omega_1\,E^2(r)dr}{\int_V E^2(r)dr}, \tag{4}$$

$$-2\frac{\omega_1-\omega_0}{\omega_0} = \frac{1}{\varepsilon_0\,\omega_0}\frac{\int_V \tilde{\sigma}_{im}\,E^2(r)dr}{\int_V E^2(r)dr} = \frac{1}{\varepsilon_0\,\omega_0}\frac{\int_V (1-\tilde{\epsilon}_{re}(r))\varepsilon_0\,\omega_1\,E^2(r)dr}{\int_V E^2(r)dr}. \tag{5}$$

The previous equations show that the frequency broadening of the resonant mode is related to the real part of the conductivity, whereas the frequency shift is related to its imaginary part. In Sec. IV, the real part of the conductivity is determined from comparison between transmission measurements and 3D-Maxwell calculations.

C. Transmission and replacement current measurements

Figure 3 shows the time evolution of the replacement current induced by an electrostatic discharge, after deconvolution by the current probe transfer function.

Figure 3 shows that the current pulse has about a 200 ns duration with a full width at half maximum (FWHM) equal to 25 ns. The transmission measurement obtained from this ESD event is presented in Fig. 4.

In Fig. 4, the electromagnetic pulse generated by the ESD in the cavity is superposed to the transmitted signal and acts as a transient perturbation. As mentioned above, the signal represented in Figs. 4(a) and 4(b) is obtained from two oscilloscope channels. Figure 4(a) is obtained without a filter, and Fig. 4(b) is obtained with a bandpass filter connected at the oscilloscope entrance with low and high cutoff frequencies equal to 0.5 and 3 GHz, respectively. The bandpass filter decreases the level of the EMP perturbation. The signals represented in Fig. 4 are characterized by an attenuation duration of about 10 μs attributed to the plasma expansion and relaxation.

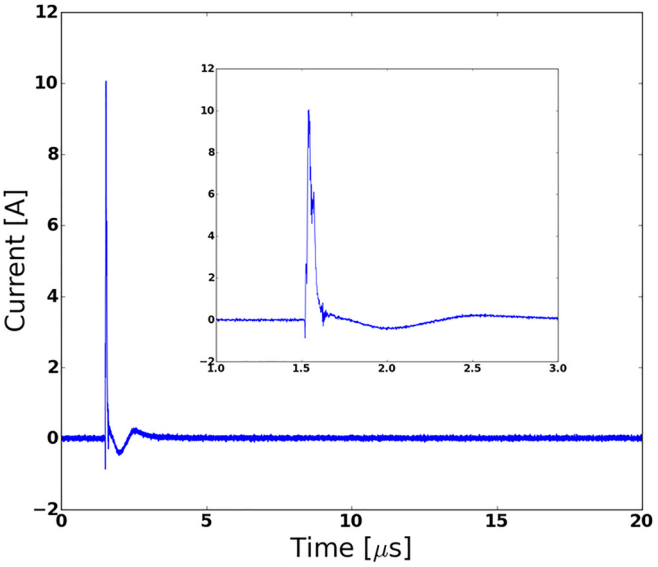

FIG. 3. Time evolution of the replacement current induced by ESD number 10 obtained from irradiation #41 in a PE sample.

Figure 5 shows the time evolution of different modes transmitted by the plasma-filled cavity. This figure is obtained by applying a Sliding Fourier Analysis (SFA) at different time windows of the signal. The SFA uses a Gaussian shape that temporally moves on the measured signal. At each time step, a Fourier analysis of the product of the measured signal with the Gaussian window is calculated. This analysis results in the time-dependent spectrum displayed in Fig. 5.

The different resonant modes of the cavity are highlighted, and it is shown that the transmission dynamics is about the same for all the different frequencies.

Figure 6 displays the transmission signal of the cavity mode at 0.8 MHz, resulting from SFA.

Figure 6 shows that the slope of the microwave signal is smoothed, which enables the accurate determination of the time evolution of the transmission signal.

Figure 7 displays some transmission signals obtained for different ESD induced plasmas produced by irradiation of polyethylene showing different values of duration and peak transmission.

Transmission measurements are characterized by a drop occurring within a characteristic time of about hundreds of nanoseconds, whereas transmission recovery occurs with a characteristic time of about a few microseconds. These transmission measurements are characterized by the transmission minimum and duration. In Fig. 8, the correlation between these characteristics is highlighted. The duration of the transmission is determined from the full width at half maximum of the absorption time evolution. Nevertheless, a correlation

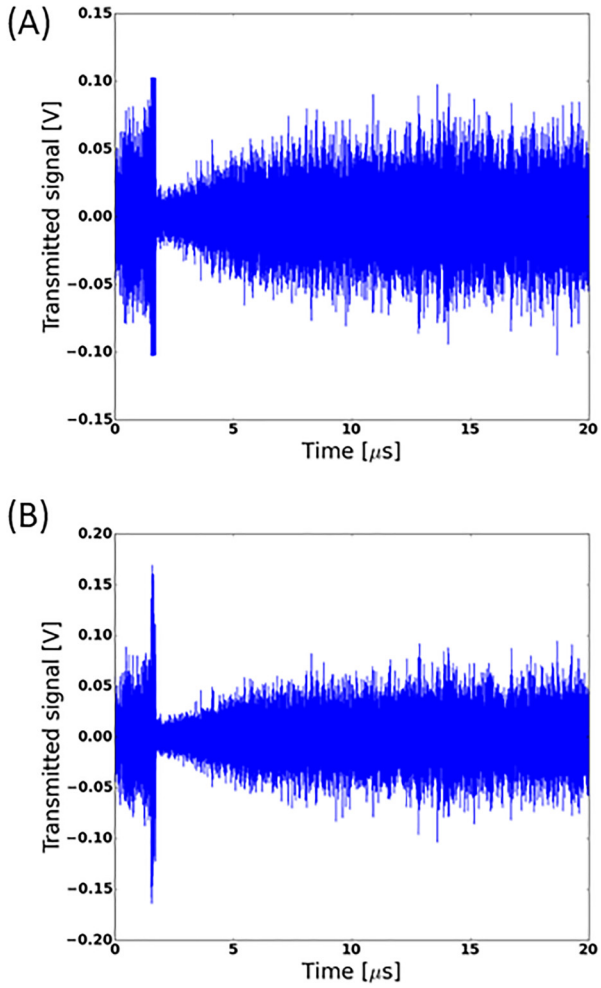

FIG. 4. Time evolution of the transmission measurement across the cavity during ESD number 10 obtained from irradiation #41 in a PE sample. (a) Raw signal. (b) Signal filtered by a (0.5–3) GHz bandpass filter.

between the maximum discharge and the minimum transmission is not observed.

Figure 8 shows that despite the large dispersion observed, a trend is put into evidence between the absorption amplitude and the duration. Discharges without plasma emission are also observed. According to the dispersion in plasma characteristics from one ESD to another, we have presented, in Fig. 9, distribution functions of the maximum of replacement current and absorption.

For PTFE and PE, each characteristic presented in Table I is quite close, and more specifically, the average absorption duration (equal to 2.1 μs) and maximum absorption (equal to 50%). These results indicate that the plasma conductivities in both materials (PE and PTFE) may be similar.

In these experiments, the incident e-beam charge and energy, and more specifically, the induced charge and energy deposition rates in the dielectric, govern the evolution of the internal electric field in the dielectric, which is the source term for dielectric breakdown and

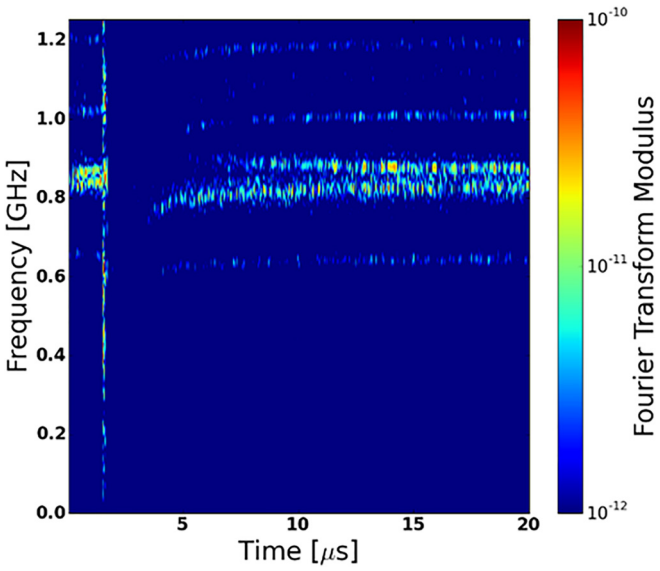

FIG. 5. Spectrogram of the signal in Fig. 4(a).

hence plasma production. The physical mechanisms involved are subsequently described. The increase in the electric field results in a competition between charge deposition by the incident e-beam and radiation induced conductivity, which is related to energy deposition by the e-beam and is responsible for the creation of a conduction current that limits the increase in the electric field. Both mechanisms (charge and energy deposition) can be obtained from the results of radiation transport calculations (taking into account for incident e-beam propagation and the production of secondary photons and electrons) by a Monte Carlo method.

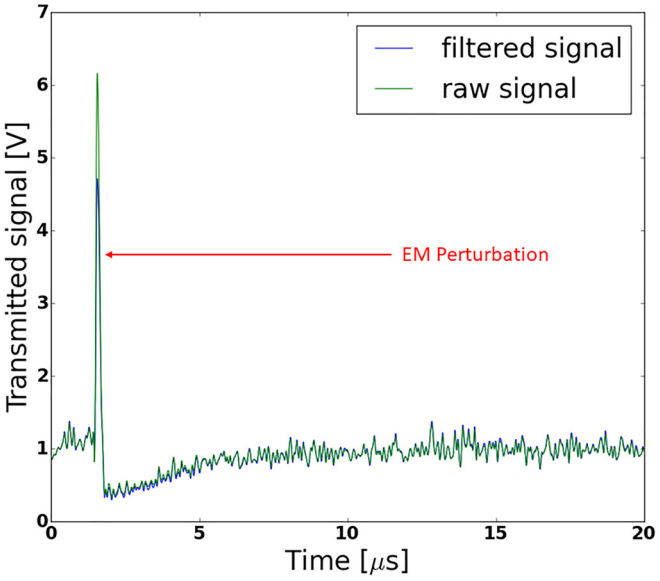

FIG. 6. SFA of the signal in Fig. 4(b).

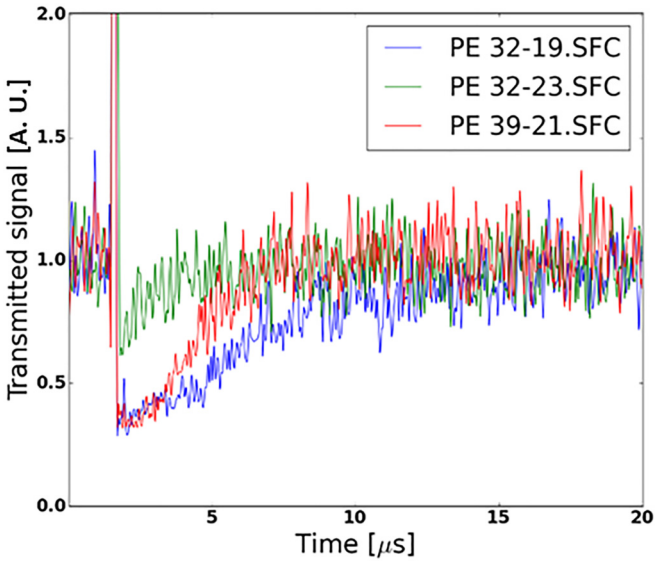

FIG. 7. Time evolutions of transmission measurements across the cavity induced by different ESDs obtained from irradiation of polyethylene.

The time and space evolution of the electric field in the dielectric can be calculated by solving Poisson and continuity equations, with charge and energy deposition rates used as source terms.[24,25]

Radiation-induced conductivity strongly depends on defects at the submillimetric scale, kinetics of radiation-induced defects, and recovering, which are related to the manufacturing processes.[15,26] These parameters lead to large uncertainties in radiation-induced conductivity and hence on disruptive threshold from a sample to another and from a manufacturer to another (the values of disruptive electric fields reported in the literature show large uncertainties[27]).

As mentioned in Sec. II, the disruptive threshold is reached in the vicinity of a small hole machined in the middle of the dielectric surface, which is in the direct view of the e-beam. This allows for controlling the location of the arc site as electric field line densities increase in

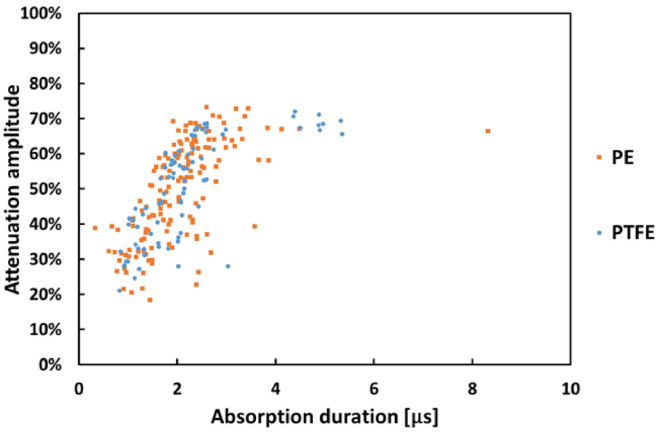

FIG. 8. Microwave transmission characteristics.

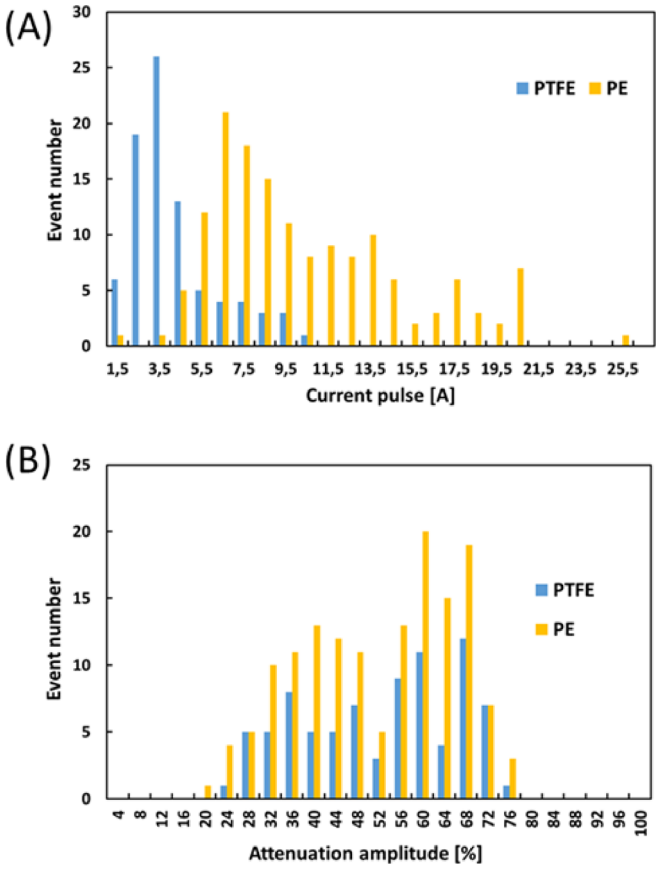

FIG. 9. Distribution functions of peak replacement current and absorption.

the machined small air cavity characterized by a smaller dielectric constant as compared to PE. This has been checked by performing irradiation of polycarbonate, which exhibits Lichtenberg patterns from the small hole.[14] Even if this caution is efficient to control the location of ESD, this does not ensure the magnitude of the electric field at breakdown, as shown by the spreading of the distributions represented in Fig. 9(a).

Once the disruptive threshold is reached, a plasma channel is produced in the dielectric, where Joule heating takes place, producing a dense plasma, which subsequently expands into vacuum.[28] Even if the measured replacement current is related to the current density of the plasma channel,[14] the above considerations show that it is difficult to precisely evaluate the disruptive electric field driving this current.

It is noteworthy that despite the uncertainties in the magnitude of the electric field at breakdown, the maximum of the replacement current distributions measured in PE and PTFE differs by a factor of 2.7 [see Fig. 9(a)]. This may be attributed to the differences between both materials of:

- the charging process leading to the value of electric field magnitude at breakdown, which is related to the spatial repartition of charge and energy deposition, and also radiation induced conductivity, defects, and recovering of the dielectric;

TABLE I. ESD and absorption signal characteristics in PE and PTFE.

Dielectric material	PE	PTFE
Number of ESD recorded	149	81
Average absorption duration (full width at half maximum) and standard deviation (μs)	2.1 ± 0.9	2.2 ± 1.1
Minimal and maximal durations of the absorption signal (μs)	0.3/8.3	0.8/5.3
Average absorption and standard deviation	50% ± 14%	50% ± 15%
Minimal and maximal absorptions	26%/81%	28%/79%
Average peak replacement current and standard deviation (A)	9.9 ± 4.6	3.7 ± 2.1
Minimal and maximal peak replacement currents (A)	1.2/25	0.8/10
Average full width at half maximum of ESD and standard deviation (ns)	30 ± 18	35 ± 32
Minimal and maximal ESD FWHM durations (ns)	4/100	3/170

- electric conductivity of the plasma channel, which is related to the kinetics of ionization, recombination, and collision frequency.

So, from our experimental results, it is not possible to quantify the mechanisms responsible for the differences in current densities of the plasma channels, and additional dielectric characterizations must be performed to state on the physical mechanisms governing these currents.

The dense plasma channel expands into vacuum according to transport equations coupled to Maxwell equations and is responsible for microwave absorption in our experiment. The fact that the distribution functions of the maximum of microwave absorption are equivalent for both dielectrics indicates that the conductivities of both expanding plasmas are similar. This may be attributed to the fact that conductivities in these expanding plasmas are governed by transport phenomena (through time and space evolution of plasma densities) rather than kinetics in the plasmas. Transport phenomena are analyzed via Maxwell simulations of the expanding plasma in Sec. III.

D. Broadband optical emission spectroscopy

Laser-Induced Breakdown Spectroscopy (LIBS) is a well-known technique to determine the composition of the irradiated material.[29,30] Samples have a known composition; for polyethylene, the C/H ratio is 0.5, and for polytetrafluoroethylene, the C/F ratio is also 0.5. In the plasma plume, this ratio can vary due to the differences in the kinetics of the different excited levels of the species densities and due to the different excitation and ionization thresholds of the different species.[31] The plasma may essentially contain radicals, monomers, and neutral and ionic species with C, F, and H elements in vacuum.[32]

In this work, broadband, low resolution, optical emission spectroscopy has been performed to infer qualitative plasma characteristics. Six Si Avalanche Photodetectors (APD120 from Thorlabs) have been set outside the cavity behind a quartz window. A bundle of six optical fibers has been set to collect the optical signal. Each fiber was connected to the photodetectors with interferential spectral filters (bandpass equal to 10 nm) set between the optical fiber termination and the Si detector.

Figure 10 represents the time evolution of the different spectral bin, set by the different filters.

Current signals occur synchronously with optical emission. As mentioned in Sec. II A, in order to control the location of the arc site, a small hole has been performed in the middle of each dielectric sample on the face in the direct view of the electron beam. These defects constrain ESD location, which is required to ensure optical signal collection by the fibers. Before each irradiation, a laser light is launched into

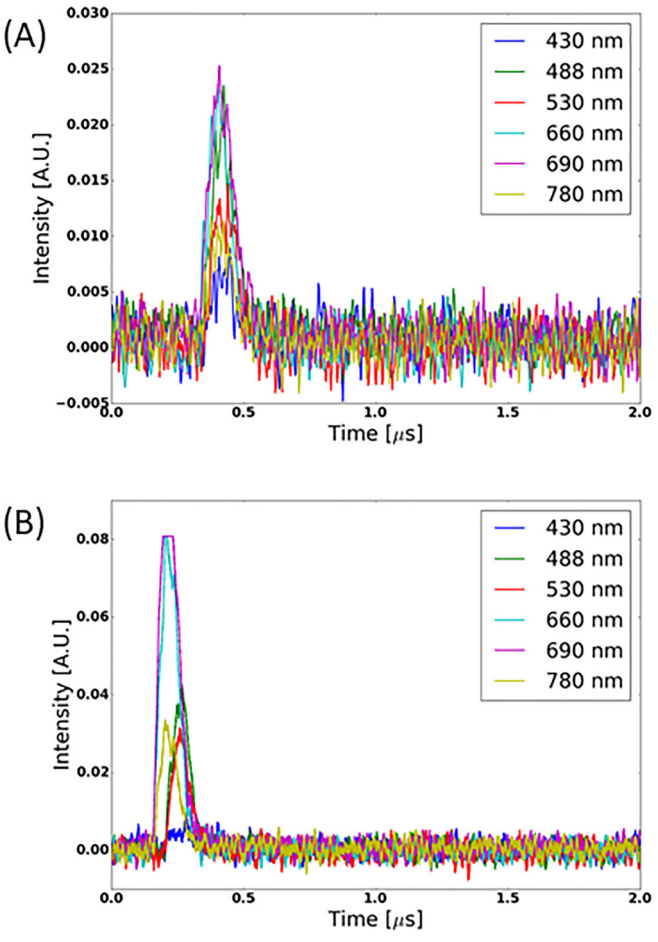

FIG. 10. Optical emission during ESD for (a) PTFE ESD #15-number 8 and (b) PE ESD #18-number 2.

each fiber at detection termination. The laser light emitted at collection termination is centered on the defect produced at the dielectric surface where ESDs occur. Figure 10 clearly indicates that a continuum is radiated by the plasma, attributed to free-free and free-bound ionic transitions. Therefore, the plasma may be highly ionized during the discharge stage (about 100 ns). So, absorption of the microwave signal is due to this expanding plasma in the cavity. In Sec. III, the electric conductivities of ESD induced plasmas are determined by the 3D-Maxwell calculations.

III. 3D MAXWELL MODELING OF MICROWAVE TRANSMISSION

A. 3D-Maxwell modeling

In this section, 3D Maxwell modeling is presented in order to analyze and to reproduce the transmission measurements presented above using a parametric analysis with the code SOPHIE developed at CEA/DAM.[33] The modeling of the cavity, as well as the generation and propagation of the microwave signal, is performed. The plasma is modeled by sampling the cavity volume with several concentric spheres around the dielectric. Two consecutive spheres defined a shell-like plasma volume, where a specific time evolution of the electric conductivity is set. The first plasma volume is a half sphere. Figure 11 represents the geometry of the cavity in the plane *xOz*, as well as the cavity sampling to define plasma volumes used for plasma modeling.

Figure 11 represents the cavity in the plane *xOz* with plasma shells, cables, and antennas to generate and detect microwave signal. The microwave signal is generated by setting a density current *J* in two half cylindrical shells at the termination of the cable located at the right of Fig. 11. The time evolution of the current density *J* set in the cable is represented in Fig. 2(a). At both cable terminations, 50 Ω resistances are set to prevent from electromagnetic field emission and induced parasitic coupling on the coaxial cable used for microwave detection. Convolutional perfectly matched layers are set to absorb electromagnetic waves and limit reflection in the calculation volume. Figure 12 represents the spatial repartition of the magnetic field module in the plane *xOz*.

Figure 12 shows that our method offers the possibility to excite the cavity modes and to simultaneously set conductivity in the cavity volume to model plasma expansion.

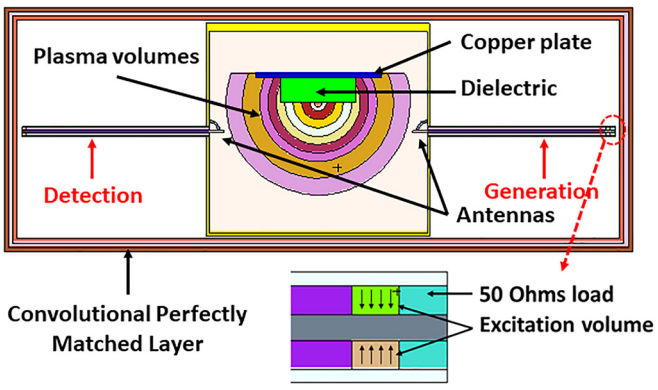

FIG. 11. Cavity modeling with plasma shells.

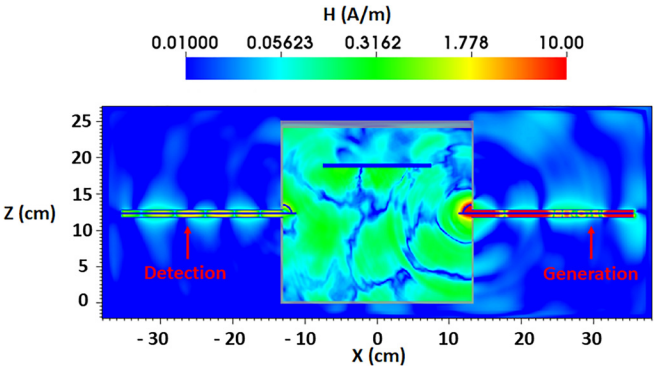

FIG. 12. Spatial distribution of the module of the magnetic field in cavity, without plasma.

B. Plasma modeling

We assume that the plasma electric conductivity has a Gaussian spatial evolution, according to the spatial evolution of plasma density determined from several theoretical models,[34,35]

$$\sigma(r,t) = \sigma_0(t) \times \exp\left[-\left(\frac{r}{r_{char}(t)}\right)^2\right], \tag{6}$$

where $r_{char}(t) = \int_{t=0}^{t} v_{expan}\,dt'$, with v_{expan} being the expansion velocity of the plasma, and $\sigma_0(t)$ is the averaged value of the plasma conductivity in the first plasma half-spherical volume (see Fig. 11), which has the form

$$\sigma_0(t) = \sigma_0 \exp\left\{-4\ln(2)\frac{(t-4t_{FWHM})^2}{t_{FWHM}^2}\right\}, \quad \text{for } t < 4t_{FWHM}, \tag{7}$$

$$\sigma_0(t) = \sigma_0 \exp\left\{-\frac{t}{t_{relax}}\right\}, \quad \text{for } t > 4t_{FWHM}, \tag{8}$$

where t_{FWHM} is the full width at half maximum, set to 75 ns, in accordance with the time evolutions of optical signals (see Fig. 10). t_{relax} is the characteristic relaxation time of the plasma conductivity, set to 2 μs.

Figure 13 shows the spatial distribution of the magnetic field module in the plane *xOz*. For this calculation, the expansion velocity v_{expan} is set to 150 km/s and $\sigma_0 = 100$ S/m.

Equation (6) shows that the expansion velocity is an important parameter of the model. To determine it, we first analyze the measured signals, which show that a transmission minimum is systematically observed at the end of the ESD, i.e., at the average values of 620 and 750 ns after the beginning of the phenomena, respectively, PE and PTFE. Furthermore, several Maxwell calculations were performed to quantify the contribution of the expanding plasma volume in the cavity to the transmission signal. For each calculation, the spatial distribution of the plasma conductivity is determined from Eqs. (6)–(8), with r ranging from $r = 0$ (the dielectric surface) to $r = r_{max}$, while it is assumed $\sigma(r,t) = 0$ for $r > r_{max}$, where r_{max} is the radius of the last plasma shell having a non-zero conductivity value. Figure 14 represents the evolution of the maximum of absorption with respect to r_{max}. In this calculation, the parameter σ_0 [see Eq. (7)] has been set to 320 S/m, in order to provide 100% absorption for r_{max}.

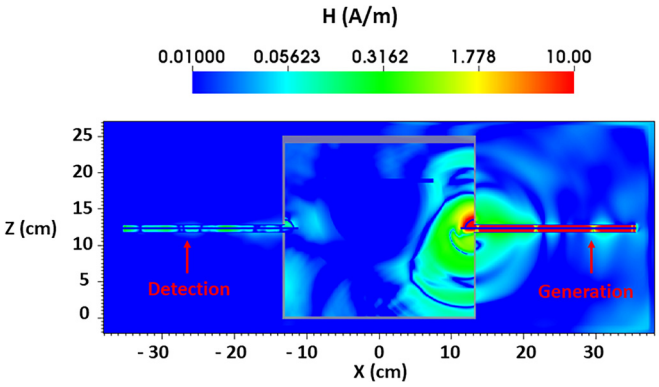

FIG. 13. Spatial distribution of the module of the magnetic field in cavity, with a plasma modeled by v_{expan}=150 km/s and σ_0 = 100 S/m, at t = 400 ns after the beginning of the ESD.

Figure 14 shows that absorption measurements can be represented by the simulation only if the plasma expands in the whole cavity. More precisely, it is observed from Fig. 14 that a plasma with a Gaussian spatial distribution as defined by Eq. (6) and extending up to ℓ_{char} = 10 cm contributes to 90% of the measured absorption. From the experimental results giving the time of minimum transmission and ℓ_{char}, the velocity of the expanding plasma is about 133 km/s from measurements with PTFE and 160 km/s from measurements with PE. These results confirm that absorption is attributed to plasma expansion rather than the expansion of Lichtenberg patterns, which are confined to the dielectric (Lichtenberg patterns were obtained in the bulk of polycarbonate samples in similar experimental conditions[14] due to deep electron implantation according to high incident electron energies).

It is noteworthy that optical diagnostics give information on the dynamic of the hotter plasma core, where the electron temperature is high enough to produce significant densities of excited states involved in the optical transitions. In the case of the ablation plasma, it has been shown that a low ionized plasma surrounds this hot core and is about twice as large as the size of the inner core.[6,36–39] So, the magnitudes of the expansion velocities determined from the optical imagery may underestimate the expansion velocity of the low ionized region of the plasma.

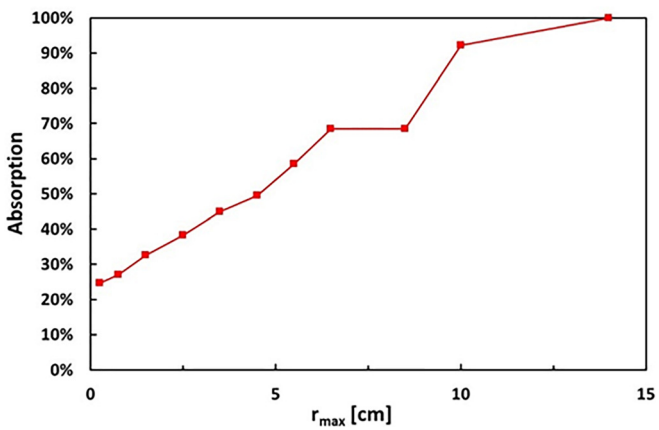

FIG. 14. Absorption with respect to plasma size r_{max}.

IV. NUMERICAL RESULTS AND ANALYSIS

A. 3D-Maxwell results

Figure 15 displays the time evolution of the measured transmission signal obtained in the case of ESD number 19 from irradiation #32 of a polyethylene sample. In addition, the time evolution of the plasma conductivity σ_0 set to simulate the measured transmission signal was plotted. The expansion velocity is fixed to 150 km/s.

We note that the measured transmission signal is not possible during the electromagnetic pulse, which is synchronous with the light emission. Consequently, the averaged conductivity in the first plasma volume deduced from the comparison between measurements and Maxwell calculations is only valid from the end of the ESD, i.e., when the plasma relaxation and expansion begin.

Figure 16 displays the evolution of the calculated absorption signal through the plasma-filled cavity with respect to the electric conductivity σ_0, in the first half-spherical plasma volume. Two plasma expansion velocities were considered: 150 km/s and 75 km/s.

From the data given in Table I, absorption measurements are in the range (25–80%), with an average value equal to 50%. This corresponds to conductivities σ_0, in the first plasma volume, in the range (2–150) S/m with an average value equal to 8 S/m, considering a plasma expansion velocity equal to 150 km/s. Fixing the expansion velocity of the plasma to 75 km/s leads to conductivities in the range $(3 \times 10^2$–$3 \times 10^4)$ S/m.

In Sec. IV B, the time evolution of the plasma conductivity determined from the Maxwell equation calculations is compared to the results of a collisional radiative model.

B. Collisional-radiative model results

A 0D Collisional-Radiative Model (CRM) describing the time-dependent evolution of the species densities of a plasma mixture containing hydrogen and carbon is used. The CRM model is described in

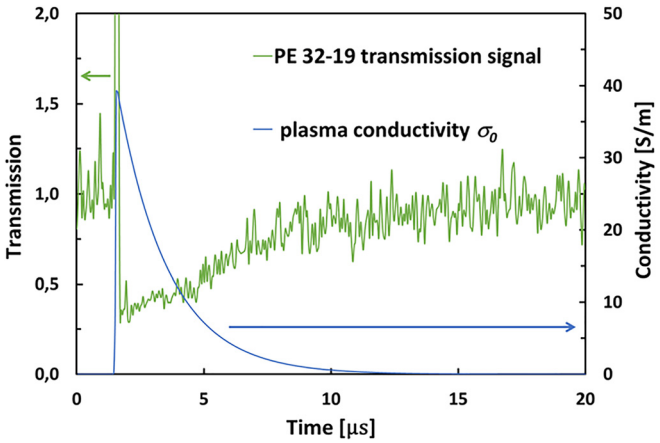

FIG. 15. Time evolution of the measured transmission signal across the cavity during ESD number 19 obtained from irradiation #32 of polyethylene sample, and the corresponding time evolution of plasma conductivity σ_0 in the first plasma volume.

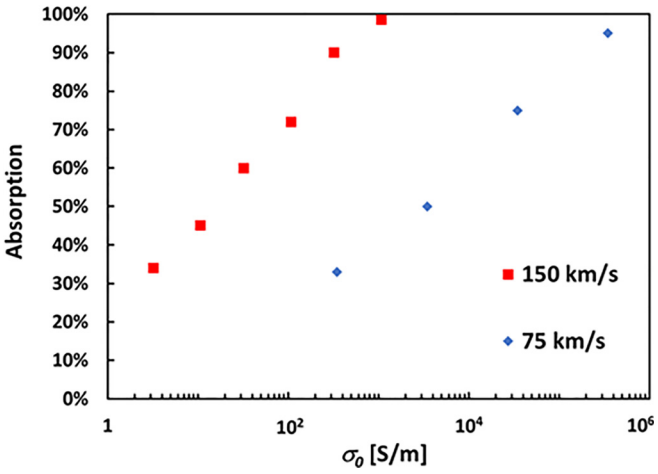

FIG. 16. Absorption with respect to σ_0, the plasma conductivity in the first volume.

detail elsewhere.[40,41] This model considers that the surface flashover rapidly desorbs molecules that are then dissociated by energetic electrons. The latter are accelerated by a high electric field (about 20 kV/mm, according to the disruptive threshold of polyethylene) creating a nonequilibrium plasma mainly composed of atomic species.

Even if during the flashover, the plasma may be highly ionized, according to the continuum emission displayed in Fig. 10, fast recombination processes occur, leading to a weakly ionized plasma expanding into the vacuum cavity. So, in the present CRM model, it is considered that a mixture of carbon and hydrogen atoms on their ground states is excited and ionized by energetic electrons.

This CRM involves 152 species, which are electrons, atoms (H and C), ions (H^-, H^+ and C^+), and their excited states, and 1408 reactions: electron-induced excitation, and ionization of ground and excited states of C; C^+ and H, electron attachment to H, and their backward or inverse reactions.

The set of basic data required to solve the CRM is calculated using nonequilibrium electron energy distribution functions (EEDFs), which have been previously determined from the solution of the multiterm Boltzmann equation[42] and pretabulated. Indeed, these EEDFs are calculated for a large range of electron average energies ε_m and for different mixtures containing hydrogen and carbon using several proportions of H and C atoms. The reaction coefficients are then calculated from these nonequilibrium EEDFs as a function of ε_m for each gas mixture.

The beginning of the simulation (t = 0 ns) corresponds to the beginning of the ESD. During its expansion, the plasma is bounded by an electronic sheath from which electrons are extracted. Each extracted electron is replaced by an electron from the plasma in order to ensure current continuity. Therefore, we assume that the current density flowing inside the plasma is equal to the current density of the discharge. Considering that the current density J_e inside the plasma is mainly electronic, it can be expressed by the following equation:

$$J_e = q n_e v_d(\varepsilon_m). \tag{9}$$

v_d is the electron drift velocity. The electron drift velocities are obtained from Boltzmann equation calculations, as a function of electron average energy ε_m. The time evolution of current density shape J_e is set to a Gaussian pulse with an FWHM 75 ns width, and the magnitude is determined from the experimental values represented in Table I. This current density crossing the surface of the first plasma volume (see Fig. 11), which is a half-sphere with a 5 mm radius, is the source term of the CRM.

Therefore, starting from an initial electron density at t and a time evolution of the current density with characteristics described above, the electron drift velocity is estimated from Eq. (9). The electron average energy ε_m(t) is deduced from v_d(t), via Boltzmann equation calculations. Then, the time evolution of the different species densities is calculated from ε_m(t) and the pretabulated reaction coefficients $K(\varepsilon_m)$.

In the following, the calculations are made with 70% H and 30% C. The main input parameter is the total initial neutral density N. The plasma conductivity in the first plasma volume is calculated from

$$\sigma_0(x) = \frac{q n_e v_d(\varepsilon_m)}{E(\varepsilon_m)}, \tag{10}$$

where $E(\varepsilon_m)$ is the electric field within the nonequilibrium plasma.

From the time of maximum electric conductivity, the evolution of the conductivity is set to an exponential law with a characteristic time equal to 2 μs, according to measurements and Maxwell calculations reported in Fig. 15,

$$\sigma_0(x) = \left.\frac{q n_e v_d(\varepsilon_m)}{E(\varepsilon_m)}\right|_{t=140\,\mathrm{ns}} \times \exp\left(-\frac{t}{t_{relax}}\right). \tag{11}$$

From this conductivity value, which is imposed in the model, the other plasma parameters such as $v_d(\varepsilon_m)$, ε_m, and the densities are inferred. Calculations are performed in order to fit the range of conductivities determined by 3D Maxwell calculations. The different parameters deduced from these calculations are summarized in Table II.

As mentioned in Sec. II C, large dispersion is observed when plotting the discharge current against minimum transmission measurements. Hence, Table II represents the results of the 0D CR model considering the whole range of conductivities and ESDs.

From the results of Table II, the mean free path λ of the electrons does not exceed the thickness of the plasma shells. This validates our model and more specifically the hypothesis of a collisional plasma in each shell defined for Maxwell calculations.

In Table II, some parameters cannot be calculated, and more precisely, when the neutral density decreases, the collision frequency decreases and hence the electron average energy increases. For example, when the electron current is fixed to 1 A, the electron average energy leading to a plasma conductivity equal to 150 S/m is much greater than 1000 eV. This leads to a mean free path much larger than the plasma shells, which involves that our model is no longer valid in these conditions.

The calculations performed with this 0D CR model allow for the determination of different plasma parameters. Figure 17 exhibits the temporal maximum of electric conductivity and average electron energy with respect to neutral density for i = 25 A.

Plasma parameters obtained from the calculations with the CRM for i = 25 A, neutral density $N = 3 \times 10^{16}$ cm^{-3} ($\sigma_0 = 40$ S/m) are displayed in Figs. 18 and 19.

The CRM gives a maximum of the electron average energy equal to 14.4 eV. This high average electron energy reported in Fig. 18 is

TABLE II. Input and output parameters of the 0D CRM calculations.

Conductivity		i = 1 A	i = 10 A	i = 25 A
$\sigma_0 = 3$ S/m	CRM input	$N = 1 \times 10^{16}$ cm^{-3}	$N = 2 \times 10^{17}$ cm^{-3}	$N = 5 \times 10^{17}$ cm^{-3}
	CRM output	$n_e = 1 \times 10^{11}$ cm^{-3}	$n_e = 2.5 \times 10^{12}$ cm^{-3}	$n_e = 7 \times 10^{12}$ cm^{-3}
		$\varepsilon_m = 15.8$ eV	$\varepsilon_m = 7$ eV	$\varepsilon_m = 6.1$ eV
		$\lambda = 123$ μm	$\lambda = 71$ μm	$\lambda = 62$ μm
$\sigma_0 = 40$ S/m	CRM input		$N = 7 \times 10^{15}$ cm^{-3}	$N = 3 \times 10^{16}$ cm^{-3}
	CRM output		$n_e = 1.1 \times 10^{12}$ cm^{-3}	$n_e = 5 \times 10^{12}$ cm^{-3}
			$\varepsilon_m = 36$ eV	$\varepsilon_m = 14.4$ eV
			$\lambda = 181$ μm	$\lambda = 117$ μm
$\sigma_0 = 150$ S/m	CRM input			$N = 5 \times 10^{15}$ cm^{-3}
	CRM output			$n_e = 2 \times 10^{12}$ cm^{-3}
				$\varepsilon_m = 63$ eV
				$\lambda = 249$ μm

consistent with the results of ESD analysis from optical spectrometry done in Ref. 32, as well as our broadband spectrometry measurements represented in Fig. 10. Figure 18 also exhibits that the total duration of electron average energy is equal to the duration of the electron current density used as the source term of the CRM. On the contrary, the electron density decreases slowly, with a characteristic time decay equal to 2 μs. This decrease is attributed mainly to the electron attachment reaction rate to H atoms and transport phenomena.

Figure 19 compares the time evolutions of the electric conductivity, in the first plasma volume, determined from the CRM and from Maxwell calculations.

Figure 19 shows that reliable results are obtained for the plasma electric conductivity with the CRM and Maxwell calculations, which validate the different assumptions of the model and, more specifically, the neutral density N and the expansion velocity.

Moreover, different gas mixture compositions have been investigated, assuming a predominant proportion of hydrogen. The considered background gas mixtures are (50% H + 50% C), (60% H + 40% C), (70% H + 30% C), and (80% H + 20% C), which affect the conductivity by 10% with a neutral density equal to 10^{16} cm^{-3}.

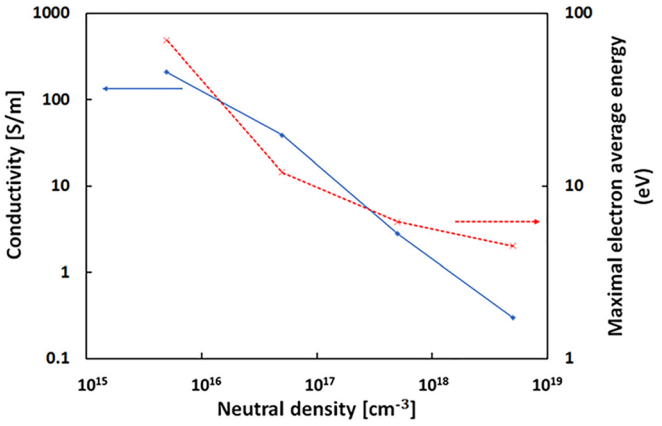

FIG. 17. Peak conductivity and electron average energy with respect to neutral density for i = 25 A.

V. CONCLUSION

In this work, a quantitative characterization of ESD-induced plasmas inside a cavity under vacuum is performed. In the first step, the electric conductivity of the plasma is determined from the comparison

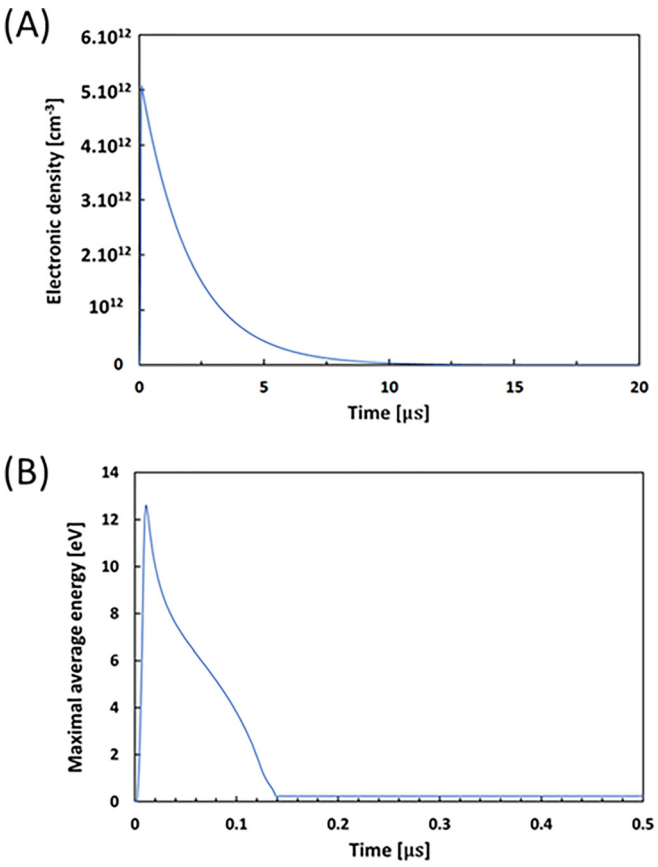

FIG. 18. Time evolution of the electron mean energy (a) and electron density (b) obtained with the CRM model for $N = 3 \times 10^{16}$ cm^{-3} and i = 25 A.

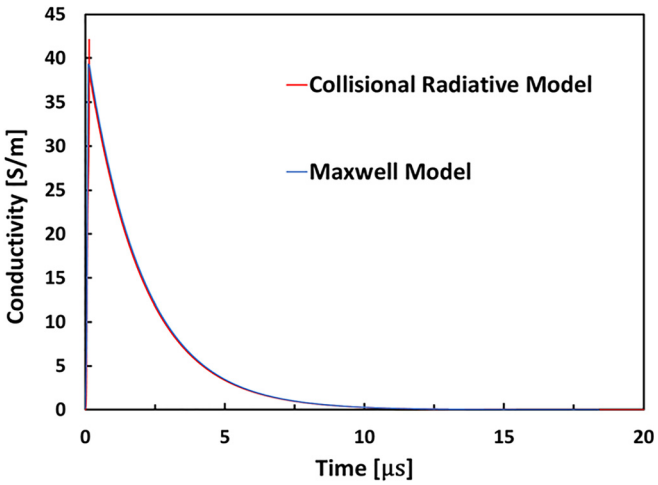

FIG. 19. Time evolution of conductivity obtained with the CRM model for $N = 3 \times 10^{16}$ cm^{-3} and i = 25 A.

between transmission measurements of a microwave signal through the cavity and 3D Maxwell calculations. The spatial evolution of the conductivity is assumed Gaussian, while the expansion velocity of the plasma is around 150 km/s, based on measurements and 3D Maxwell calculations.

A CRM model is also used to fit the time evolution of the conductivity in the first plasma volume. It highlights the importance of attachment reactions and transport to decrease electron density within a characteristic time of about few microseconds. Moreover, the CRM model restitutes some plasma parameters such as the neutral species densities desorbed by the discharge (between 10^{16} and 10^{18} cm^{-3}), the electron average energies (between 5 and 60 eV), and the electron densities (between 10^{12} and 10^{13} cm^{-3}).

These results are important to perform a precise characterization of the electromagnetic constraints associated with the electrostatic discharge for satellite hardening. Moreover, the method of plasma characterization reported in this work may be used to validate experimental as well as numerical determination of thermal and mechanical constraints induced by the discharges, and related material vulnerability to these effects.

ACKNOWLEDGMENTS

This work was supported by the Direction Générale de l'Armement (DGA) of the French Ministry of Defense and by the Région Occitanie. The authors thank G. Assaillit, C. Delbos, A. Garrigues, and D. Aubert for their support on experimental activities.

REFERENCES

[1]E. Monteil, N. Demaria, L. Pacher, A. Rivetti, M. Dionisio Da Rocha Rolo, R. Whealdon, A. Paternò, and S. Panati, "600 Mrad TID effects on a new generation high rate pixel readout ASIC in 65 nm CMOS with low-power, low noise synchronous analog front-end using fast ToT encoding and auto-zeroing," in 17th European Conference on Radiation and its Effects on Components and Systems (2017).
[2]J. L. Leray, S. Bazzoli, J.-E. Sauvestre, and Y. V. Glebov, "Evidence for a radiation induced electromotive force (RIEMF) in dielectrics exposed to very high 14 MeV neutron flux by means of neutron induced recoils," IEEE Trans. Nucl. Sci. **55**(6), 3060–3069 (2008).
[3]J.-L. Dubois, F. Lubrano-Lavaderci, D. Raffestin, J. Ribolzi, J. Gazave, A. Compant La Fontaine, E. d'Humières, S. Hulin, P. Nicolaï, A. Poyé, and V. T. Tikhonchuk, "Target charging in the short pulse laser-plasma experiments," Phys. Rev. E **89**(1), 013102-1–013102-15 (2014).
[4]R. Maisonny, M. Ribière, M. Toury, J. M. Plewa, M. Caron, G. Auriel, and T. d'Almeida, "Investigating the performances of a 1 MV high pulsed power linear transformer driver: From beam dynamics to x radiation," Phys. Rev. Accel. Beams **19**, 120401-1–120401-9 (2016).
[5]J. M. Plewa, V. Bernigaud, T. Barnes, F. Poulet, A. Georges, R. Delaunay, M. Ribière, C. Vermare, M. Yousfi, O. Eichwald, T. d'Almeida, and R. Maisonny, "High power electron diode for linear induction accelerator at a flash radiographic facility," Phys. Rev. Accel. Beams **21**, 070401 (2018).
[6]M. Ribière, R. Maisonny, and T. d'Almeida, "Numerical and experimental characterization of a plasma induced on a solid target by an intense pulsed multi-MeV e-beam," Phys. Plasmas **24**, 063105 (2017).
[7]M. Ribière, S. Demarquay, M. Maulois, R. Maisonny, T. D'Almeida, M. Toury, B. Crabos, C. Gonzalez, A. Garrigues, C. Delbos, and B. Azaïs, "Contribution of electromagnetic perturbation to the transient response of an electronic circuit exposed to a high multi-MeV x-ray flux," IEEE Trans. Nucl. Sci. **62**(3), 1383–1394 (2015).
[8]H. C. Koons, J. E. Mazur, R. S. Selesnick, J. B. Blake, J. F. Fennell, J. L. Roeder, and P. C. Anderson, "The impact of space environment on space systems," Aerospace Report No. TR-99 (1670)-1, Aerospace Corporation, El Segundo, Los Angeles, CA (1999).
[9]P. D. Fieseler, S. M. Ardalan, and A. R. Frederickson, "The radiation effects on Galileo spacecraft systems at Jupiter," IEEE Trans. Nucl. Sci. **49**, 2739 (2002).
[10]B. Gross, "Radiation-induced conductivity in Teflon irradiated by x-rays," J. Appl. Phys. **52**(2), 571 (1981).
[11]K. Yahagi and A. Danno, "Gamma-ray induced conductivity in polyethylene and Teflon under radiation at high dose rate," J. Appl. Phys. **34**(4), 804 (1963).
[12]A. R. Frederickson, E. G. Holeman, and E. G. Mullen, "Characteristics of spontaneous electrical discharging of various insulators in space radiations," IEEE Trans. Nucl. Sci. **39**(6), 1773–1782 (1992).
[13]N. W. Green and J. R. Dennison, "Deep dielectric charging of spacecraft polymers by energetic protons," IEEE Trans. Plasma Sci. **36**(5), 2482–2490 (2008).
[14]T. Gouriou, M. Ribiere, D. Aubert, O. Eichwald, and M. Yousfi, "Numerical and experimental characterizations of currents and magnetic fields produced by electrostatic discharges within dielectrics irradiated by high-energy electron flux," IEEE Trans. Plasma Sci. **47**, 3766 (2019).
[15]R. Hanna, T. Paulmier, P. Molinie, M. Belhaj, B. Dirassen, D. Payan, and N. Balcon, "Radiation-induced conductivity in space dielectric materials," J. Appl. Phys. **115**, 033713 (2014).
[16]D. Aubert, G. Assaillit, G. Auriel, C. Delbos, A. Garrigues, F. de Gaufridy, L. Labarbe, D. Plouhinec, A. Queiros, P. Ribeiro, M. Ribière, S. Ritter, and A. Rizzon, "A 6 MeV electron LINAC facility for multipurpose radiation testing," in Proceedings of the 16th RADECS Conference (2016).
[17]I. Jun, H. B. Garrett, and R. W. Evans, "Trapped particle environments of the outer planets," Trans. Plasma Sci. **47**, 3923 (2019).
[18]See www.spenvis.oma.be for "DICTAT (Dielectric Internal Charging Threat Assessment Tool)."
[19]See https://www.nist.gov for NIST Database.
[20]M. N. Spencer, J. S. Dickinson, and D. J. Eckstrom, "Afterglow conductivity measurements of air and N2 following intense electron-beam excitation," J. Phys. D **20**, 923 (1987).
[21]M. Ribière, T. d'Almeida, O. Cessenat, M. Maulois, R. Pouzalgues, B. Crabos, C. Delbos, A. Garrigues, and B. Azais, "Investigation of the electron density of multi-MeV X-ray-induced air plasmas at low pressures based on electromagnetic resonant cavity analysis," Phys. Plasmas **23**, 122106 (2016).
[22]G. Neumann and U. Bänziger, Rev. Sci. Instrum. **64**, 19 (1993).
[23]M. A. Heald and C. B. Wharton, *Plasma Diagnostics with Microwaves*, 1st ed. (Wiley, 1965).
[24]A. R. Frederickson, "Electric discharges pulses in irradiated solid dielectrics in space," IEEE Trans. Electr. Insul. **EL18**, 337 (1983).
[25]K. G. Balmain and G. R. Dubois, "Surface discharges on Teflon, Mylar and Kapton," IEEE Trans. Nucl. Sci. **26**, 5146 (1979).

[26]Th. Baumann, B. Fruth, F. Stucki, and H. R. Zeller, "Field-enhancing defects in polymeric insulators causing dielectric aging," IEEE Trans. Electr. Insul. **24**, 1071 (1989).
[27]*Handbook of Chemistry and Physics*, edited by J. R. Rumble (CRC Press, 2018–2019), ISBN: 978-1138367296.
[28]R. B. Miller, "Mechanism of explosive electron emission for dielectric fiber (velvet) cathodes," J. Appl. Phys. **84**, 3880 (1998).
[29]G. Koren and J. T. C. Yeh, "Emission spectra and etching of polymers and graphite irradiated by excimers lasers," J. Appl. Phys. **56**, 2120 (1984).
[30]D. Rusak, K. Weaver, and B. Taroli, "Laser-induced breakdown spectroscopy for analysis of chemically etched polytetrafluoroethylene," Appl. Spectrosc. **62**, 773 (2008).
[31]R. Sattmann, I. Monch, H. Krause, R. Noll, S. Couris, A. Hatziapostolou, A. Mavramanolakis, C. Fotakis, E. Larrauri, and R. Miguel, "Laser-induced breakdown spectroscopy for polymer identification," Appl. Spectrosc. **52**, 456 (1998).
[32]B. Vayner, D. C. Ferguson, and J. T. Galofaro, "Emission spectra of arc plasmas," IEEE Trans. Plasma Sci. **36**, 2219–2227 (2008).
[33]M. Ribiere, T. Gouriou, O. Eichwald, M. Yousfi, and B. Azais, "Reduced kinetics model for X-ray-generated atmospheric air plasmas fitted by microwave transmission measurements," J. Appl. Phys. **125**, 083303 (2019).
[34]P. Mora, "Collisionless expansion of a Gaussian plasma into a vacuum," Phys. Plasmas **12**, 112102 (2005).
[35]M. Murakami and M. N. Basko, "Self-similar expansion of finite-size non-quasi-neutral plasmas into vacuum: Relation to the problem of ion acceleration," Phys. Plasmas **13**, 012105 (2006).
[36]M. Ribière, B. G. Chéron, and A. Bultel, High Temp. Mater. Processes **12**, 111 (2008).
[37]M. Ribière, D. Karabourniotis, and B. G. Chéron, "Spectroscopic analysis of the excitation transfer from background air to diffusing aluminum laser produced plasma," J. Appl. Phys. **105**, 083309 (2009).
[38]D. Karabourniotis, M. Ribiere, and B. G. Cheron, "Electron temperature and density determination in a nonequilibrium laser induced plasma by means of self-reversed-line spectroscopy," Appl. Phys. Lett. **93**, 041501 (2008).
[39]D. Karabourniotis, M. Ribière, and B. G. Chéron, "Impact of ion-quasistatic broadening on the determination of the electron density in a laser-induced plasma from line self-reversal," J. Phys. D **42**, 105202 (2009).
[40]J.-M. Plewa, O. Eichwald, M. Yousfi, M. Ribiere, and R. Maisonny, "Reduced time-dependent collisional-radiative models of non-equilibrium plasmas produced by surface flashover on a velvet cathode," J. Phys. D **51**, 284005 (2018).
[41]J.-M. Plewa, O. Eichwald, M. Yousfi, G. Wattieaux, S. Cartier, F. Cartier, F. Poulet, V. Bernigaud, M. Ribiere, R. Delaunay, T. d'Almeida, and R. Maisonny, "Modeling and experimental characterization of the plasma produced by a velvet cathode in a linear induction accelerator," Phys. Plasmas **25**, 083506 (2018).
[42]M. Yousfi and M. D. Benabdessadok, "Boltzmann equation analysis of electron-molecule collision cross sections in water vapor and ammonia," J. Appl. Phys. **80**(12), 6619–6631 (1996).